ADVANCED OPTICAL MATERIALS
www.advopticalmat.de

Ruddlesden–Popper and Dion–Jacobson Perovskites in Multiple Quantum Wells Light-Emitting Diodes

*Shir Yudco and Lioz Etgar**

Low dimensional perovskite forms multiple quantum wells (MQWs) structures that can be an efficient structure for light-emitting diodes (LEDs). Here the use of different barrier molecules is demonstrated to create Ruddlesden–Popper and Dion–Jacobson 2D perovskite and implement them in LEDs. It is found that the aromatic barrier molecules are better performing in Perovskite LED (PeLED) compared to linear barrier molecules. The benzylammonium (BnzA), $n = 5$, shows the highest external quantum efficiency (EQE) of 16.65% compared to the di-ammonium and the linear barrier molecules. The BnzA forms $n = 1$ inside the 3D perovskite, which provides a non-radiative energy transfer from the wider bandgap, $n = 1$ perovskite, to the smaller bandgap, 3D perovskite, that presents radiative recombination. Optical characterizations support the MQW structure whereas physical characterizations show unique morphology of separate nanocrystals laying on top of thin perovskite film during the $n = 5$ BnzA crystallization. In addition, it is revealed that the barrier molecule type, in this case, the BnzA, is responsible for the formation of the MQW structure whereas other barrier molecules didn't show this structure. The formation of an additional low *n*-value phase inside the 3D perovskite is beneficial for the enhancement of the radiative recombination which results in high EQE.

1. Introduction

In the last decade, hybrid perovskite proved to be a leading candidate to be used in photovoltaic and optoelectronic devices. The efficiency of perovskite-based solar cells increased from 3.8% in 2009[1] to more than 25%[2] today. Hybrid perovskite has attractive interesting properties such as relatively high charge carrier mobility compared to organic materials,[3] long carrier lifetime,[4] high photoluminescence quantum yield (PLQY),[5,6] and tunable bandgap with the ability to achieve high color purity[7] which led to the development of perovskite light-emitting diodes (PeLEDs). The first development of PeLEDs started in 2014 demonstrating 0.1% external quantum efficiency (EQE),[8] reaching today more than 28%[9] due to vast research and developments of the PeLEDs device structure,[10] defect passivation,[11] and the reduction of non-radiative recombination.[12] In addition, electron and hole blocking layers,[13,14] passivation layers,[15,16] additive combinations,[17] and transferred to low dimensionality[18] are used in order to further develop PeLEDs.

The perovskite dimensionality can be changed from the typical 3D structure with the chemical formula of AMX_3, where A is a small monovalent cation (typically MA, FA or Cs), M is a divalent metal cation (most commonly Pb) and X is a halide anion (I, Br or Cl), into a 2D or quasi-2D structure where A is a large cation that doesn't fit into the octahedral cage. The large A cation separates the inorganic octahedrons forming 2D sheets of perovskite. In 2D perovskite, the large organic cation (also called the barrier molecule) has a low dielectric constant in comparison to the relatively high dielectric constant of the lead halide octahedral layers[19,20,21] which enhances the quantum well structure in the 2D perovskite.

Using a mixture of the small and the large cations, one can form a quasi-2D structure made of 3D layers quantumly confined by a layer of the barrier molecule. The number of confined 3D layers (referred to as the "*n*" value) is determined by the stoichiometric ratio between the two cations. In the case of high "*n*" values the perovskite layer is contained from a mixture of "*n*" values, ranging between $n = 1$ and the stoichiometric "*n*" value, leading to a unique energy structure of multiple quantum wells (MQW) that can lead to energy transfer to the narrower bandgap in the structure.[18,22,23] This property is beneficial for PeLED since it can reduce exciton dissociation and nonradiative recombination by overcoming trapping in sub-bandgap levels, enhancing radiative recombination, and improving the PeLED performance.[12,24,25]

The common types of 2D perovskites are the Ruddlesden-Popper (RP) perovskite with a monoamine organic cation as the barrier molecule according to the chemical formula: $(R\text{-}NH_3)_2(A)_{n-1}M_nX_{3n+1}$, (**Figure 1**b). Alternatively, by using a di-amine organic cation as the barrier molecule a Dion-Jacobson

S. Yudco, L. Etgar
Institute of Chemistry
Casali Center for Applied Chemistry and the Center for Nanoscience and Nanotechnology
The Hebrew University of Jerusalem
Jerusalem 91904, Israel
E-mail: lioz.etgar@mail.huji.ac.il

The ORCID identification number(s) for the author(s) of this article can be found under https://doi.org/10.1002/adom.202302592

DOI: 10.1002/adom.202302592

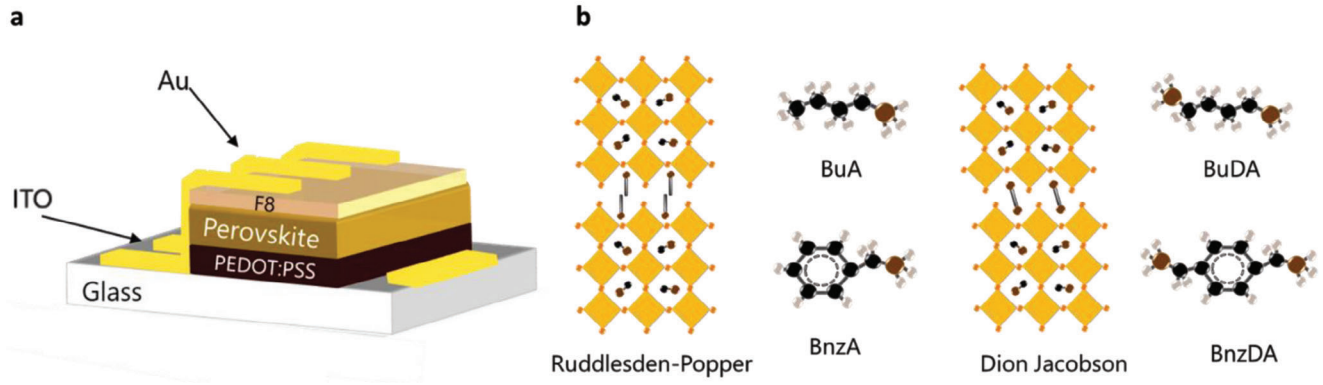

Figure 1. Schematic illustration of (a) the PeLED device architecture fabricated in this work, b) quasi-2D perovskite structure: (left) Ruddlesden–Popper perovskite with the monoamine cations, butylammoniun (BuA), and benzylammonium (BnzA), (right) Dion–Jacobson perovskite with the diamine cations used in this work 1,4-butanediammonium (BuDA) and,4-benzenedimethanammonium (BnzDA).

(DJ) perovskite structure can be formed according to the chemical formula $(NH_3\text{-R-}NH_3)(A)_{n-1}M_nX_{3n+1}$ (Figure 1b).

Choosing different barrier molecules will change both the interactions inside the lattice of the perovskite as well as the distance between the 3D layers leading to different confinement effects and inherent changes to the perovskite layer.[26,27] The common barrier molecules have an amine group that interacts with the inorganic lead halide octahedral, and a long organic tail, most commonly an alkyl chain or an aromatic ring. In monoamine barrier molecules with long alkyl chains, the main interactions between the barrier molecules are van der Waals, while aromatic barrier molecules will form strong π-π stacking interactions.

In this work, we used 2D perovskite in LED devices, we carefully studied the role of the barrier molecule type on the PeLEDs performance. We used four different barrier molecules, where two of them formed RP 2D perovskite while the others formed DJ 2D perovskite. It is hypothesized that the van der Waals or π-π stacking interactions could influence the PeLED performance. In order to elucidate the difference in the performance of the LEDs, we performed several optical and physical characterizations which shed more light on the mechanism of the devices.

2. Results and Discussion

Four barrier molecules were studied in 2D perovskite ($n = 5$) and implemented as the emitting layer inside the LED devices. In order to understand the effect of the low dimensional perovskite on the LED performance parameters, apart from the 2D perovskite layer, all other layers remained the same for all devices. The LED structure is based on the inverted structure having the following architecture: ITO/ (PEDOT: PSS)/Perovskite/MoO_3 doped F8/Au as illustrated in Figure 1a. (PEDOT:PSS- Poly(3,4-ethylenedioxythiophene) polystyrene sulfonate, F8- Poly(9,9-di-n-octylfluorenyl-2,7-diyl)).

The Four barrier molecules can be seen in Figure 1b, namely: butylammoniun (BuA), 1,4-butanediammonium (BuDA), benzylammonium (BnzA), and 1,4-benzenedimethanammonium (BnzDA). The rationale behind choosing these barrier molecules is based on three parameters: i) linear and aromatic barriers, ii) monoammonium and diammonium, iii) and having approximately the same length. Based on the barrier molecule type (i.e., monoammonium or diammonium) the perovskite composition will change, where using the chemical formula $(R\text{-}NH_3)_2(MA)_{n-1}Pb_nBr_{3n+1}$, for the Ruddlesden-Popper (RP) structure and $(NH_3\text{-R-}NH_3)(MA)_{n-1}Pb_nBr_{3n+1}$ for the Dion-Jacobson perovskite (DJ) structure. The deposition conditions for the perovskite layer were optimized for each barrier molecule, changing the perovskite solvent, concentration, and spin conditions to improve the device efficiency. Importantly the electron transporting layer (ETL) and the hole transporting layer (HTL) were not fully optimized for each perovskite type in order to elucidate the role of the perovskite layer on the device functionality.

The LED devices were measured by applying a voltage scan and simultaneously measuring the current density and light emission. **Figure 2** presents the EL measurements of the PeLEDs for all four barrier molecules. As can be seen, the performance of the devices was affected by the change in the barrier molecule. The Luminescence intensity in Watt m^{-2} can be seen in Figure 2a, where the BnzA shows the highest EL intensity, achieving up to 0.52 W m^{-2} with an average intensity of 0.4 W m^{-2}. BnzDA reached 0.11 W m^{-2} with an average intensity of 0.07 W m^{-2}, while the linear barriers had significantly lower intensities, with an average EL intensity of 0.003 W m^{-2} for BuDA and 0.0006 W m^{-2} for BuA. Changes in the current density of the devices show different trends than the EL trend, as can be seen in Figure 2b. The average current density, which is measured at the point where the EQE is the highest, shows 212 mA cm^{-2} for BnzA, 160 mA cm^{-2} for BnzDA, 351 mA cm^{-2} for BuA, and 101 mA cm^{-2} for BuDA. The external quantum efficiency (EQE) is calculated by dividing the number of emitted photons by the number of injected electrons, therefore, to understand the changes in device performance it is important not just to follow the EQE but also to study the luminescence intensity and current density throughout the measurement.

Figure 2c–f presents the EL intensity and the current density versus the applied bias for the different barrier molecules. By comparing the two trends at the same points of measurement one can learn about the radiative and non-radiative processes occurring in the device. The measurement of the BnzA in Figure 2c shows a leakage current at 2 V (the JV curve) already before the radiative recombination is started which occurs at 3 V (the EL curve). The leakage current is significantly reduced at 4 V (JV

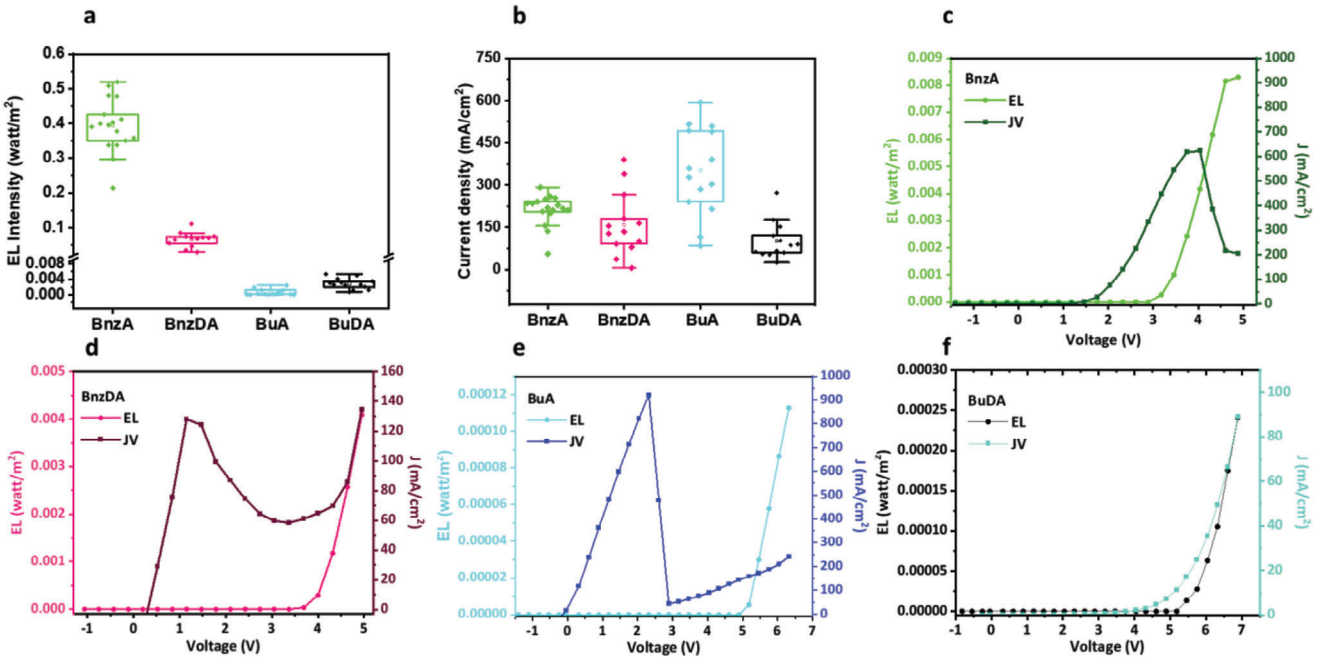

Figure 2. Electroluminescence (EL) measurements of the PeLEDs using the studied barrier molecules. a) EL intensity measured in watt m^{-2}; b) Current density in mA cm^{-2}. Current density and EL intensity versus voltage for the devices with the different barrier molecules: c) BnzA, d) BnzDA, e) BuA, and f) BuDA.

curve) due to strong radiative recombination as can be seen by the EL curve.

In the case of BnzDA devices (Figure 2d) a high leakage current can be observed already from 0.4 V, yet the reduction in the leakage current does not correlate to the radiative recombination, indicating that a non-radiative recombination process occurs in the device already from low voltages. This observation can assist in explaining the decrease in the EL intensity between BnzA and BnzDA as can be seen in Figure 2a. The leakage current and non-radiative process are more dominant in BuA (Figure 2e), which shows a leakage current that starts at 0 V and a strong non-radiative process at 2.3 V. The radiative process in the BuA device starts at a high voltage of 5.2 V, leading to the lowest luminescence intensity values.

Leakage current and non-radiative recombination create heat release in the device that can cause joule heating. As a result, the device operation can be harmed in several ways, first, the joule heat can affect the organic layers in the device due to relatively lower thermal stability,[28] second in combination with high current density it can create non-balanced charge injection leading to Auger recombination, reducing the device efficiency as well as increasing the turn-on voltage.[29] The only barrier molecule that did not show any leakage current is BuDA (Figure 2f) however, the radiative recombination is not efficient compared to the other barrier molecules, leading to low luminescence intensity values, indicating strong non-radiative processes in the device.

In addition to the changes in the EL intensity and current density, a difference in the emission wavelength and turn-on voltage was observed. **Figure 3**a presents the wavelength of the EL peak center for each barrier molecule, the change in the peak position is related to the barrier molecule length. Due to variation in the dielectric constant of the barrier molecules a multiply quantum well (MQW) structure is formed inside the perovskite layer,[24] where for each barrier molecule this MQW structure is slightly different which influences the confinement and affects the bandgap of the perovskite forming a shift in the EL wavelength. As a result, one can achieve high color purity, covering a wide range of different green light emissions simply by changing the barrier molecule in the 2D perovskite. The color changes can be seen in the Commission Internationale de l'Eclairage (CIE) color coordinates (Figure 3b), with chromaticity coordinates of (0.3043,0.6642) for BnzA, (0.2335,0.7931) for BnzDA, (0.2007,0.7700) for BuA, and (0.0799, 0.7913) for BuDA. An additional important parameter that changes between the barrier molecules is the turn-on voltage (V_{on}) as can be seen in Figure 3c (stated as emission voltage). The turn-on voltage provides the point where the first radiative recombination was recorded by photon emission, indicating the voltage required to achieve a balanced charge injection into the perovskite layer. All the barrier molecules show a relatively high V_{on} of over 3 V, reaching 3.0, 4.2, 5.0, and 5.3 V for BnzA, BnzDA, BuA, and BuDA respectively. The difference in the V_{on} can be related to i) the semiconducting organic ETL (F8) and HTL (PEDOT: PSS) which reduce the charge mobility in the device,[29] and ii) the joule heating, as mentioned previously, leading to higher turn-on voltages.[28,29]

Figure 3d presents the EQE of all barrier molecules. As was mentioned earlier, the EQE is determined from the luminescence and current density, therefore similar trend can be expected to be observed between the EL results (Figure 1a) and the EQE (Figure 3d). The BnzA reached the best EQE of 16.65% with an average EQE of 9.8% while BnzDA, BuA, and BuDA reached an average EQE of 2.4%, 0.01%, and 0.16% respectively. It can be observed that the best-performing device also demonstrated the lowest V_{on}, which can indicate the device

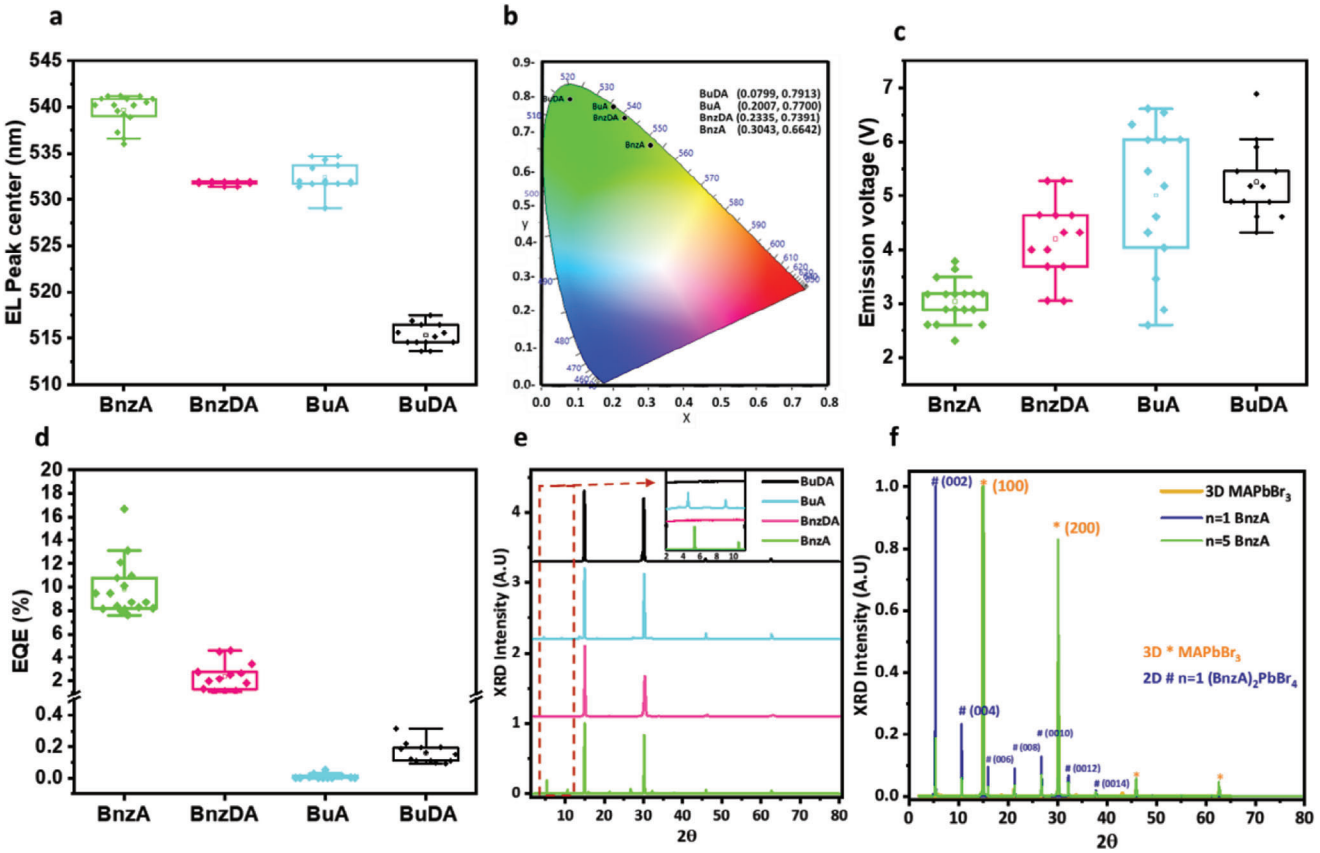

Figure 3. Electroluminescence (EL) parameters of PeLEDs with the different barrier molecules. a) Wavelength at the center of EL peak; b) CIE chromaticity coordinates; c) Emission voltage (turn on voltage), the voltage applied during the bias scan on the LED where the first EL was recorded; d) External Quantum Efficiency (EQE) of the PeLED. XRD measurements for e) all barrier molecules with enlargement of the low angles peaks (inset); f) comparison between 3D $MAPbBr_3$, 2D $n = 1$ $(BnzA)_2PbBr_4$, and 2D $n = 5$ $(BnzA)_2(MA)_4Pb_5Br_{16}$.

efficiency dependence on the band alignment, as was discussed in Figure 3a. The change in the bandgap of the perovskite according to the barrier molecules, influences the band alignment needed to achieve a balanced charge injection, a poor band alignment will increase the V_{on} (Figure 3c) and will also cause joule heating and non-radiative charge recombination as can be seen in Figure 2c–f. Based on the results so far it can be assumed that partial contribution to the better performance in the case of BnzA is related to a better energy band alignment of the perovskite layer and the selective contacts. The connection between the barrier molecule and the device efficiency extends to the device stability (Figure S6, Supporting Information), the devices were tested under consecutive measurements, applying cycles of 0 to 5 V while tracking the LED efficiency. LEDs based on the linear molecules, which showed low efficiency (Figure 3d) were unstable and did not withstand more than one consecutive measurement. The aromatic barriers that performed well as LEDs (Figure 3d) were measured for 10 consecutive measurements, BnzA devices maintained 80% of their original efficiency, while BnzDA decreased below 1% efficiency after 10 consecutive measurements, indicating the superior performance of BnzA

In order to further investigate the reason for the significant change in the EQE between the barrier molecules, and especially the reason that BnzA devices performed extremely well, further characterizations were performed on the perovskite films. Figure 3e presents XRD measurements where the main phase that was detected for $n = 5$ perovskite with the different barrier molecules is the 3D $MAPbBr_3$ phase. In the monoammonium barrier molecules (BnzA and BuA) additional peaks were observed at low angles indicating strong confinement of the low dimensional perovskite (Figure 3e inset). However, the peaks in the case of BuA were shifted from the expected 2D perovskite phase, while for BnzA the additional peaks at low angles match perfectly the $n = 1$ perovskite, $BnzAPbBr_4$, as can be seen in more detail in Figure 3f. All the peaks in the XRD spectrum of $n = 5$ BnzA were matched to either 3D $MAPbBr_3$ or 2D $n = 1$ $BnzAPbBr_4$.

The additional $n = 1$ perovskite which is present in the BnzA $n = 5$ is also observed in the absorbance spectra. (**Figure 4**a) The BnzA absorbance spectrum shows a clear peak at ≈400 nm related to a lower "n" value inside the perovskite, which can not be observed in the other barrier molecules with the same $n = 5$. Figure 4b shows the absorbance spectra of $n = 1$ and $n = 5$ of BnzA as well as 3D $MAPbBr_3$. This confirms that the additional peak ≈400 nm is related to $n = 1$ which formed just in the case of the BnzA films. The multiple energy gaps in quasi-2D perovskite are a result of the formation of a multiple quantum well system (MQW) made by a changing energy landscape throughout the perovskite layer with different bandgap domains.

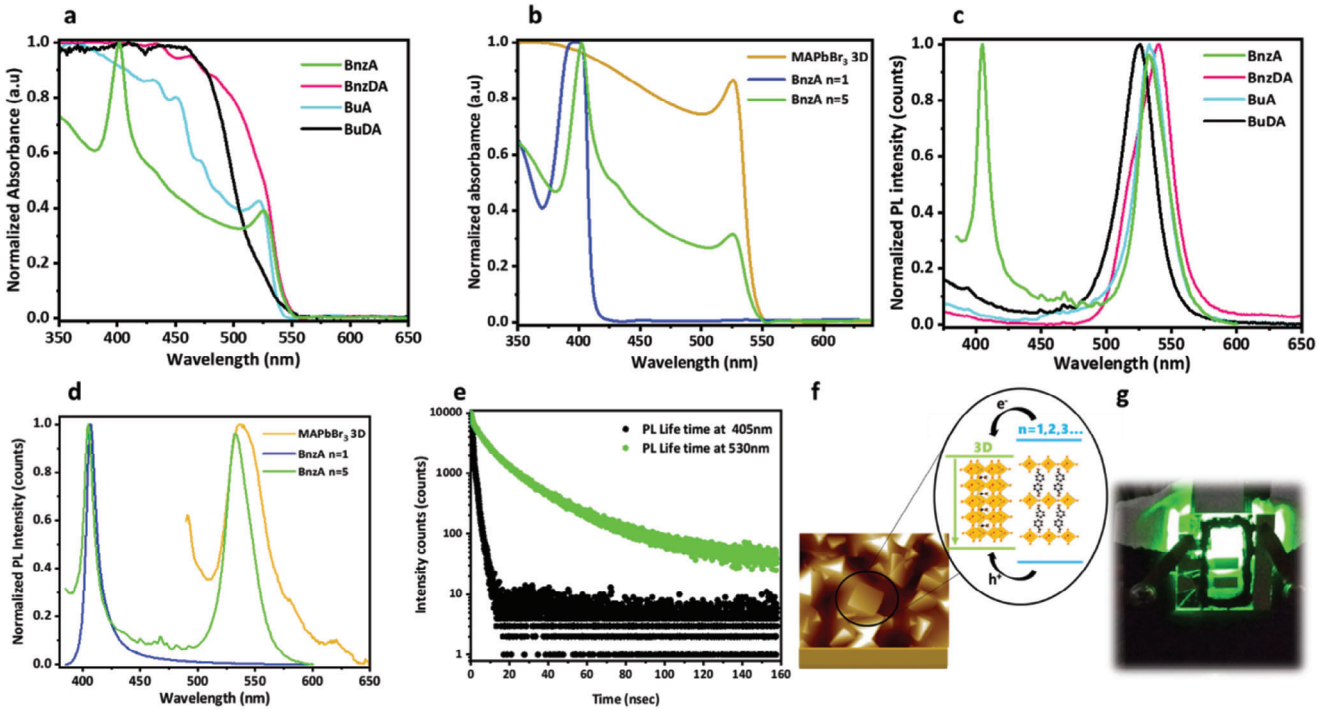

Figure 4. Optical properties: absorbance and photoluminescence (PL) measurements for a,c) all barrier molecules; b,d) comparison between 3D $MAPbBr_3$, 2D $n = 1$ $(BnzA)_2PbBr_4$ and quasi 2D $n = 5$ $(BnzA)_2(MA)_4Pb_5Br_{16}$. e) Photoluminescence lifetime measurements for quasi 2D $n = 5$ $(BnzA)_2(MA)_4Pb_5Br_{16}$ at two wavelength 405 nm, trucking emission from the $n = 1$ phase, and 530 nm for the 3D phase. f) Schematic illustration of the non-radiative charge transfer between wide and narrow bandgaps inside the perovskite layer. f) Picture of $n = 5$ BnzA PeLED emission during EL measurements.

To further verify the presence of the two phases in the BnzA, (one with high dimensionality and the second with low dimensionality), the PL spectra of all the barrier molecules were investigated. As can be seen in Figure 4c a single peak was measured for BnzDA, BuA, and BuDA, matching their EL peak and absorbance onset (Figure S1, Supporting Information), indicating an emission from the bandgap of the material. Interestingly, BnzA was the only one that presented two different peaks, showing emission from two different confined energy levels. As was seen in the absorbance and XRD measurements, the first peak at 533 nm correlates with the EL peak (Figure S1a, Supporting Information) of 3D perovskite, and the second at 405 nm belongs to the emission from n = 1 $BnzAPbBr_4$. It is important to mention that the second PL peak at 405 nm doesn't appear in the EL spectrum of the LED (the reason for that is discussed below). Figure 4d compares the PL of $n = 1$ $BnzAPbBr_4$ film, $n = 5$ $(BnzA)_2MA_4Pb_5Br_{16}$ film, and 3D $MAPbBr_3$ film, which agree well with the previous characterizations of the presence of both $n = 1$ and 3D inside the BnzA $n = 5$ layer.

This unique structure for the BnzA might be responsible for the improvement in the device EQE. The confinement of two different bandgaps can lead to a mechanism of non-radiative energy transfer from the wide bandgap ($n = 1$) to the narrow bandgap (3D) as illustrated schematically in Figure 4f. Increasing the charge concentration in the 3D domains allows it to overcome the fast charge diffusion to the grain boundaries and defect traps and efficiently increases the radiative recombination over non-radiative trap-assisted charge recombination processes that can lead to a loss in the device efficiency.[30,31] This results in a single peak at the EL spectrum (Figure S1a, Supporting Information) with improved radiative recombination due to the inhibition of the non-radiative recombination,[18] leading to high luminescence intensity as can be seen by the measured values in Figure 1a and the picture in Figure 4g.

The evidence for non-radiative energy transfer can also be supported by the PL lifetime measurements as shown in Figure 4e. The PL lifetime of the BnzA was detected at two different emission wavelengths according to their PL peaks. The observed PL lifetime was significantly different, where a longer PL lifetime was observed for the 3D peak (15.9 ns) compared to a shorter PL lifetime (1 ns) for the 2D $n = 1$ peak (see Table S1, Supporting Information), which is due to the transfer of excited charges to the lower energy level, leading to a very short recombination lifetime at the wider bandgap.[24] In addition to the optical measurements which provide us with the suggested mechanism for the high EQE of BnzA, detailed physical characterizations including top-view SEM, cross-section FIB, and AFM were performed. Top view SEM images revealed a significant change in the perovskite morphology, BnzA morphology (Figure S2a, Supporting Information) shows cubic crystals on top of the perovskite surface, the cubic grains seem to be separated on top of a smooth perovskite surface, in comparison BnzDA surface also shows crystalline grain on the surface (Figure S2c, Supporting Information) but the crystals are not separated. The same morphologies can be seen in the AFM measurement in Figure S2b,d (Supporting Information). In the linear barriers the crystalline phase is not

observed, BuA shows a smooth surface with large grain boundaries and pinholes throughout the layer (Figure S2e, Supporting Information) that can be seen clearly in the AFM images (Figure 2SF, Supporting Information), while BuDA shows a nonuniform layer with small grains and a lot of pinholes (Figure S2g,f, Supporting Information). In addition to the top-view SEM, the full LED devices of the different barrier molecules were taken for a cross-section made by a focused ion beam (FIB) where the images were taken by HR-SEM.

The cross-section images (Figures S3a–d, Supporting Information) support the observation made from the SEM top view images. In the case of the linear barrier molecules the pin-holes in the layers are dominant, in Figure S3c (Supporting Information) the perovskite layer of BuA is absent from several parts of the device, where holes were also observed at the top view SEM and AFM, which explains the poor device efficiency. Due to the pin-holes the ETL and the HTL are touching each other, leading to a strong leakage current and non-radiative recombination process as discussed above (Figure 2e). In the case of BuDA, there are smaller holes in the perovskite layer, and most of the device area is covered by a nonuniform perovskite layer with variation in thickness, explaining the significant reduction in the radiative recombination of the device (Figure 2f). In the case of the aromatic barrier molecules, the textured surface seen in the SEM and the AFM is apparent with clearer grain boundaries. The grains on the surface of the layer act as recombination sites assisting to enhance the radiative recombination.[32,33] This explains the improved performance of the LEDs which are based on these barrier molecules, small grains can reduce exciton diffusion length, therefore decreasing exciton dissociation and improving radiative recombination.[34,35] The cross-section image of BnzA (Figure S3a, Supporting Information) shows a unique submicrometer scale structure that crystalized spontaneously during the spin coating process. The formation of these sub-micrometer crystallites in the film is rarely formed spontaneously by spin coating of bulk perovskite,[36] which can improve the light emission by reducing light trapping in the perovskite layer that hinders the device performance. Light trapping can have a significant effect on PeLEDs due to the relatively high refractive index, and the sub-micrometer crystallites. This can lead to a change in the refractive index throughout the layer that can extract wide-angle light from the perovskite film[37] increasing the luminescence intensity and EQE (as seen in Figures 2a and 3d). In order to verify that the origin of the two phases in BnzA is related to the barrier molecule and not as a result of specific deposition conditions, PeLEDs were fabricated for all barrier molecules using the same perovskite's deposition conditions that were found optimal for BnzA.

During the work, each PeLED device was fabricated using the optimal perovskite solvents, concentration, and spin conditions. In the case of BnzA, only DMSO was used as a solvent contrary to the other barrier molecules. The use of DMSO as the only solvent for the perovskite solution slows down the perovskite crystallization since the DMSO evaporates during the device annealing compared to DMF which evaporates during the spin coating of the perovskite layer.[38,39,40] Based on these observations, in order to verify the effect of the film fabrication method on the device performance two experiments were performed, first devices with BnzA were fabricated using four different solvent ratios: only DMSO, 1:4 DMF: DMSO, 1:1 DMF: DNSO, and 4:1 DMF: DMSO. As expected the best PeLED performance was observed only for the DMSO as the perovskite's solvent. Absorbance and PL measurements of these solvents ratios can be observed in Figure S4a,b (Supporting Information). In all solvent ratios, the strong confinement for the low and high dimensionality was observed. Second, devices of all the barrier molecules using the same optimal conditions of BnzA with DMSO as the only solvent were fabricated. The EQE of these devices using BnzDA, BuA, and BuDA was very low. Also in the absorbance and the PL, the 2D $n = 1$ phase did not appear (Figures S4c,d, Supporting Information). The absorbance measurements of all the barrier molecules with DMSO as the only solvent show strong confinement in comparison to the optimal solvents used for these barrier molecules (Figure S4c, Supporting Information). However, these measurements didn't show any formation of $n = 1$ phase. The only case where $n = 1$ was observed is for BnzA. In addition, top-view SEM images of perovskite films of all the barrier molecules fabricated at the same conditions as the BnzA, presented in Figure S5 (Supporting Information), reveal different film morphology depending on the barrier molecule. These additional experiments support the conclusion that the formation of the two quantum-confined phases is a result of the use of BnzA as the barrier molecule and not the change in the perovskite's deposition conditions.

3. Conclusion

This work concentrates on low-dimensional perovskite implemented in LED. Mono-ammonium and di-ammonium linear and aromatic barrier molecules were studied. The BnzA barrier molecule demonstrates the highest EQE compared to the other barrier molecules. It was found that the BnzA formed a 2D $n = 1$ perovskite phase in addition to the 3D phase which formed in $n = 5$ perovskite. Absorbance and PL show the existence of $n = 1$ peak at 400 nm in addition to the 3D peak at 550 nm, which is also supported by XRD. PL lifetime of the BnzA demonstrates a longer lifetime for the 3D peak compared to a much shorter lifetime for the 2D $n = 1$ peak, due to the transfer of excited charges to the smaller bandgap, leading to a very short recombination lifetime at the wider bandgap. Morphology was unique in the case of BnzA having separate perovskite crystals on top of a smooth thin perovskite layer which assists in the radiative recombination. Finally, it was shown that the deposition conditions don't affect the two-phase formation in the case of BnzA, and that depends solely on the specific barrier molecule being used. This work demonstrates the importance of the barrier molecule on the device performance due to the multi-quantum well structure.

4. Experimental Section

Barrier Molecule Synthesis: Barrier molecule synthesis was conducted by slowly dripping hydrobromic acid (48wt.% in water, Aldrich) in excess to a solution of the barrier amine precursor (benzylamine Aldrich 99%, butylamine Aldrich 99.5%, 1,4-Diaminobutan Acros 99%, and p-Xylylenediamine Aldrich 99%) in ethanol absolute. The precipitate was washed three times in diethyl ether (Bio-Lab) and recrystallized with ethanol absolute (Holland Moran 99.8%).

Preparation of Perovskite Solutions: Preparation of perovskite solutions was performed in a nitrogen-filled glovebox by dissolving stoichiometric

quantities amounts according to the RP or DJ chemical formula (as specified in the introduction) of the synthesized barrier molecule, MABr (GreatCell Solar Company) and $PbBr_2$ (Aldrich ≥98%). The solutions were dissolved in different ratios of dimethyl sulfoxide (DMSO, Aldrich 99.7% extra dry) and Dimethyl formamide (DMF, Aldrich anhydrous 99.8%). The solvent ratios and concentrations were determined based on device optimizations. Using 1 M in only DMSO for BnzA, 1.2 M in 1:4 DMSO DMF ratio for BnzDA, 0.8 M in 2:3 DMSO: DMF ratio for BuA, and 1 M in 4:1 DMSO: DMF ratio for BuDA. The perovskite solution was heated overnight at 60 °C.

Device Fabrication: The devices were fabricated on Indium Tin Oxide (ITO) conductive glass (15 Ω, Automatic Research) substrates, cleaned by four cycles of sonication baths using Hellmanex (2%), deionized water, acetone, and ethanol, and 15 min of oxygen plasma treatment. Poly(3,4-ethylenedioxythiophene) polystyrene sulfonate (PEDOT: PSS) (Al 4083 Ossila) was deposited on the clean substrates by dynamic spin coating at 6000 rpm for 30 s and annealed at 140 °C for 15 min, then treated with ethanol absolute and deionized water solution in a 4:1 ratio, at 4000 rpm for 40 s and annealed at 120 °C for 5 min. The perovskite deposition was performed in a nitrogen-filled glovebox. BnzA, BuA, and BuDA solutions were spin-coated at 3000 rpm for 30 s, and BnzDA solution was spin-coated at 1000 rpm for 10 s followed by 5000 rpm for 60 s followed by 20 min of annealing at 100 °C. Next Poly(9,9-di-n-octylfluorenyl-2,7-diyl) (F8) (Aldrich) was dissolved in 1 mg to 75 µL of Chlorobenzene (CB, Aldrich 99.8% extra dry), and spin-coated at 3000 rpm for 30 s, then MoO_3 was thermally evaporated in vacuum of ≈10-7 Torr for 125 s followed by thermal evaporation of 70 nm Au metal contact.

Electroluminescence: Electroluminescence (EL) measurements were a combination of two simultaneous measurements, emission measurements, and current-voltage (*I–V*) measurements. *I–V* curves measurements were performed using the Keithley model 2400 digital source meter. EL measurements were performed using F1000-VISNIR optic fiber with cosine receptor, StellarNet BLACK-Comet Spectrometer with CRX-100 partially depleted absorber photodetector.

X-Ray Diffraction: X-ray Diffraction (XRD) measurements were performed on a D8 Advance diffractometer (Bruker AXS, Karlsruhe, Germany) with a secondary graphite monochromator, 2° Soller slits, and a 0.2 mm receiving slit. XRD patterns ranging from 2 to 75° 2θ were recorded at room temperature using CuKa radiation (l = 1.5418 Å) with the following measurement conditions: a tube voltage of 40 kV, a tube current of 40 mA, a step-scan mode with a step size of 0.02° 2θ, and a counting time of 1 s per step.

Absorbance: Absorbance measurements were performed using a Jasco V-670 UV–vis-NIR spectrophotometer.

Photoluminescence (PL) and PL Lifetime: Photoluminescence (PL) and PL lifetime measurements were performed for perovskite films on microscope glass, using Horiba Fluoromax-4 spectrofluorometer. The device operates with a 150 W CW Ozone-free xenon arc lamp. Excitation grating of 1200 groove mm^{-1} blazed at 330 nm. Emission grating of 1200 groove mm^{-1} blazed at 500 nm and Photomultiplier detector. PL lifetime was measured at 405 and 530 nm using a 375 nm nanoLED excitation.

Scanning Electron Microscopy: Scanning Electron Microscopy (SEM) measurements were performed using Magellan Extra High-Resolution SEM using a FEI (field emission instruments), The Netherlands. The measurement conditions were 5 kV.

Atomic Force Microscopy Measurements: Atomic Force Microscopy (AFM) measurements were performed using Dimension Icon XR Scanning Probe Microscope (Bruker, USA) Images were acquired in Tapping Mode, using RTESP-300 probes, Bruker (spring constant 42 N m^{-1}, frequency 300 kHz).

Focused Ion Beam and Ultrahigh Resolution Scanning Electron Microscopy: Focused Ion Beam (FIB) and Ultrahigh Resolution Scanning Electron Microscopy (UHR-SEM) measurements were performed by placing the samples inside a FEI Helios Nano Lab 460F1 and excavated using a focused gallium-ion beam to expose the layered structure. The layered stack was tilted to 52.0° and imaged on a separate holder. The image conditions were 2 kV, 0.1nA, and the detector was through the lens detector (TLD).

Supporting Information

Supporting Information is available from the Wiley Online Library or from the author.

Acknowledgements

The authors would like to thank the Israel Ministry of Energy and the Israel Science Foundation for their financial support. This research was also partially supported by grants from the National Research Foundation, Prime Minister's Office, Singapore under its Campus of Research Excellence and Technological Enterprise (CREATE) program.

Conflict of Interest

The authors declare no conflict of interest.

Data Availability Statement

The data that support the findings of this study are available in the supplementary material of this article.

Keywords

EQE, LED, low dimensional perovskite, quantum well

Received: October 30, 2023
Revised: November 22, 2023
Published online:

[1] A. Kojima, K. Teshima, Y. Shirai, T. Miyasaka, *J. Am. Chem. Soc.* **2009**, *131*, 6050.
[2] NREL, *Photovolt. Res.* **2023**.
[3] D. Shi, V. Adinolfi, R. Comin, M. Yuan, E. Alarousu, A. Buin, Y. Chen, S. Hoogland, A. Rothenberger, K. Katsiev, Y. Losovyj, X. Zhang, P. A. Dowben, O. F. Mohammed, E. H. Sargent, O. M. Bakr, *Science* **2015**, *347*, 519.
[4] C. Wehrenfennig, G. E. Eperon, M. B. Johnston, H. J. Snaith, L. M. Herz, *Adv. Mater.* **2014**, *26*, 1584.
[5] S. D. Stranks, H. J. Snaith, *Nat. Nanotechnol.* **2015**, *10*, 391.
[6] X.-K. Liu, W. Xu, S. Bai, Y. Jin, J. Wang, R. H. Friend, F. Gao, *Nat. Mater.* **2021**, *20*, 10.
[7] L. Peng, J. Geng, L. Ai, Y. Zhang, R. Xie, W. Yang, *Nanotechnology* **2016**, *27*, 335604.
[8] Z.-K. Tan, R. S. Moghaddam, M. L. Lai, P. Docampo, R. Higler, F. Deschler, M. Price, A. Sadhanala, L. M. Pazos, D. Credgington, F. Hanusch, T. Bein, H. J. Snaith, R. H. Friend, *Nat. Nanotechnol.* **2014**, *9*, 687.
[9] Z. Liu, W. Qiu, X. Peng, G. Sun, X. Liu, D. Liu, Z. Li, F. He, C. Shen, Q. Gu, F. Ma, H.-L. Yip, L. Hou, Z. Qi, S.-J. Su, *Adv. Mater.* **2021**, *33*, 2103268.
[10] Z. Wei, J. Xing, *J. Phys. Chem. Lett.* **2019**, *10*, 3035.
[11] J. Ye, M. M. Byranvand, C. O. Martínez, R. L. Z. Hoye, M. Saliba, L. Polavarapu, *Angew. Chem.* **2021**, *133*, 21804.
[12] H. Cheng, Y. Feng, Y. Fu, Y. Zheng, Y. Shao, Y. Bai, *J. Mater. Chem. C* **2022**, *10*, 13590.
[13] R. Quintero-Bermudez, J. Kirman, D. Ma, E. H. Sargent, R. Quintero-Torres, *J. Phys. Chem. Lett.* **2020**, *11*, 4213.

[14] D. Bin Kim, J. C. Yu, Y. S. Nam, D. W. Kim, E. D. Jung, S. Y. Lee, S. Lee, J. H. Park, A. Y. Lee, B. R. Lee, D. Di Nuzzo, R. H. Friend, M. H. Song, *J. Mater. Chem. C* **2016**, *4*, 8161.
[15] X. Yang, X. Zhang, J. Deng, Z. Chu, Q. Jiang, J. Meng, P. Wang, L. Zhang, Z. Yin, J. You, *Nat. Commun.* **2018**, *9*, 570.
[16] N. Kim, M. Shin, S. Jun, B. Choi, J. Kim, J. Park, H. Kim, W. Jung, J.-Y. Lee, Y.-H. Cho, B. Shin, *ACS Appl. Mater. Interfaces* **2021**, *13*, 37323.
[17] M. Ban, Y. Zou, J. P. H. Rivett, Y. Yang, T. H. Thomas, Y. Tan, T. Song, X. Gao, D. Credgington, F. Deschler, H. Sirringhaus, B. Sun, *Nat. Commun.* **2018**, *9*, 3892.
[18] L. Zhang, C. Sun, T. He, Y. Jiang, J. Wei, Y. Huang, M. Yuan, *Light Sci Appl* **2021**, *10*, 61.
[19] D. B. Mitzi, *J. Chem. Soc. Dalton Trans.* **2001**, 1.
[20] J. Calabrese, N. L. Jones, R. L. Harlow, N. Herron, D. L. Thorn, Y. Wang, *J. Am. Chem. Soc.* **1991**, *113*, 2328.
[21] O. Yaffe, A. Chernikov, Z. M. Norman, Y. Zhong, A. Velauthapillai, A. Van Der Zande, J. S. Owen, T. F. Heinz, *Phys Rev B Condens Matter Mater Phys* **2015**, *92*, 045414.
[22] N. Wang, L. Cheng, R. Ge, S. Zhang, Y. Miao, W. Zou, C. Yi, Y. Sun, Y. Cao, R. Yang, Y. Wei, Q. Guo, Y. Ke, M. Yu, Y. Jin, Y. Liu, Q. Ding, D. Di, L. Yang, G. Xing, H. Tian, C. Jin, F. Gao, R. H. Friend, J. Wang, W. Huang, *Nat. Photonics* **2016**, *10*, 699.
[23] D. Shin, F. Zu, E. R. Nandayapa, L. Frohloff, E. Albert, E. J. W. List-Kratochvil, N. Koch, *Adv. Funct. Mater.* **2023**, *33*, 2208980.
[24] M. Yuan, L. N. Quan, R. Comin, G. Walters, R. Sabatini, O. Voznyy, S. Hoogland, Y. Zhao, E. M. Beauregard, P. Kanjanaboos, Z. Lu, D. H. Kim, E. H. Sargent, *Nat. Nanotechnol.* **2016**, *11*, 872.
[25] T. Goto, H. Makino, T. Yao, C. H. Chia, T. Makino, Y. Segawa, G. A. Mousdis, G. C. Papavassiliou, *Phys Rev B Condens Matter Mater Phys* **2006**, *73*, 115206.
[26] T. L. Leung, I. Ahmad, A. A. Syed, A. M. C. Ng, J. Popovic, A. B. Djurisic, *Commun. Mater.* **2022**, *3*, 63.
[27] D. Ghosh, D. Acharya, L. Pedesseau, C. Katan, J. Even, S. Tretiak, A. J. Neukirch, *J. Mater. Chem. A* **2020**, *8*, 22009.
[28] Y. Sun, Q. Su, H. Zhang, F. Wang, S. Zhang, S. Chen, *ACS Nano* **2019**, *13*, 11433.
[29] K. Qasim, B. Wang, Y. Zhang, P. Li, Y. Wang, S. Li, S.-T. Lee, L.-S. Liao, W. Lei, Q. Bao, *Adv. Funct. Mater.* **2017**, *27*, 1606874.
[30] L. Cheng, T. Jiang, Y. Cao, C. Yi, N. Wang, W. Huang, J. Wang, *Adv. Mater.* **2020**, *32*, 1904163.
[31] L. N. Quan, Y. Zhao, F. P. García De Arquer, R. Sabatini, G. Walters, O. Voznyy, R. Comin, Y. Li, J. Z. Fan, H. Tan, J. Pan, M. Yuan, O. M. Bakr, Z. Lu, D. H. Kim, E. H. Sargent, *Nano Lett.* **2017**, *17*, 3701.
[32] R. Kumar, J. Kumar, P. Srivastava, D. Moghe, D. Kabra, M. Bag, *ACS Appl. Mater. Interfaces* **2020**, *12*, 34265.
[33] J. Qin, J. Zhang, Y. Bai, S. Ma, M. Wang, H. Xu, M. Loyd, Y. Zhan, X. Hou, B. Hu, *iScience* **2019**, *19*, 378.
[34] H. Cho, S.-H. Jeong, M.-H. Park, Y.-H. Kim, C. Wolf, C.-L. Lee, J. H. Heo, A. Sadhanala, N. Myoung, S. Yoo, S. H. Im, R. H. Friend, T.-W. Lee, *Science* **2015**, *350*, 1222.
[35] Z. Xiao, R. A. Kerner, L. Zhao, N. L. Tran, K. M. Lee, T.-W. Koh, G. D. Scholes, B. P. Rand, *Nat. Photonics* **2017**, *11*, 108.
[36] J. A. Sichert, Y. Tong, N. Mutz, M. Vollmer, S. Fischer, K. Z. Milowska, R. García Cortadella, B. Nickel, C. Cardenas-Daw, J. K. Stolarczyk, A. S. Urban, J. Feldmann, *Nano Lett.* **2015**, *15*, 6521.
[37] Y. Cao, N. Wang, H. Tian, J. Guo, Y. Wei, H. Chen, Y. Miao, W. Zou, K. Pan, Y. He, H. Cao, Y. Ke, M. Xu, Y. Wang, M. Yang, K. Du, Z. Fu, D. Kong, D. Dai, Y. Jin, G. Li, H. Li, Q. Peng, J. Wang, W. Huang, *Nature* **2018**, *562*, 249.
[38] W. S. Yang, J. H. Noh, N. J. Jeon, Y. C. Kim, S. Ryu, J. Seo, S. I. Seok, *Science* **2015**, *348*, 1234.
[39] W. Li, J. Fan, J. Li, Y. Mai, L. Wang, *J. Am. Chem. Soc.* **2015**, *137*, 10399.
[40] S. Yudco, A. S. Dayan, B.-E. Cohen, T. Binyamin, L. Etgar, *J. Mater. Chem. C* **2022**, *10*, 10037.